Optical Design and Analysis of the Submillimeter-Wave Instrument on JUICE

Mikko Kotiranta, *Member, IEEE*, Karl Jacob, Hyunjoo Kim, Paul Hartogh, and Axel Murk

***Abstract*—The submillimeter-wave instrument on the Jupiter icy moons explorer spacecraft is a passive dual-beam heterodyne radiometer operating in the frequency bands 530–625 and 1080–1275 GHz. The instrument will observe Jupiter's atmosphere as well as the atmosphere and surface properties of its moons. This paper presents the optical design and analysis of the instrument that has been carried out using Gaussian beam mode analysis and physical optics simulations. The optics consists of a 29-cm mechanically steerable off-axis Cassegrain telescope, relay optics, and two feedhorns. Frequency-independent operation of the 600-GHz channel is predicted by the simulations. The 1200-GHz channel shows some frequency dependency because of the selected feedhorn type. The steering of the telescope affects mainly its cross-polarization level. The manufacturing and mounting tolerances, as well as distortion and misalignment by thermoelastic effects, will cause the performance of a real instrument to deviate from that of an ideal one. Physical optics simulations combined with data from finite-element method simulations and measurements of optical surface profiles show that these factors affect, in particular, the instrument pointing. The induced pointing error is up to several arcminutes, whereas the specification is less than 0.5 arcmin. The pointing error can be reduced by adjusting the alignment of the telescope secondary mirror and the feedhorns.**

***Index Terms*—Monte Carlo, optical design, physical optics (PO), quasi-optics, radiometers, submillimeter-wave instrument, tolerance analysis.**

I. Introduction

THE Jupiter ICy moons Explorer (JUICE) is an ESA large-class mission to Jupiter and its satellites. The launch is scheduled for 2022. The spacecraft carries ten instruments onboard, one of them being the submillimeter-wave instrument (SWI) that is a passive dual-beam heterodyne radiometer for the frequency bands 530–625 and 1080–1275 GHz [1]. The telescope and receiver unit (TRU) of the instrument is depicted in Fig. 1. Additionally, the instrument consists of an electronic unit with different high-resolution and broadband spectrometers and a radiator unit that allows passive cooling of the Schottky diode mixers and low-noise amplifiers of the receiver unit (RU) to a temperature of 120 K.

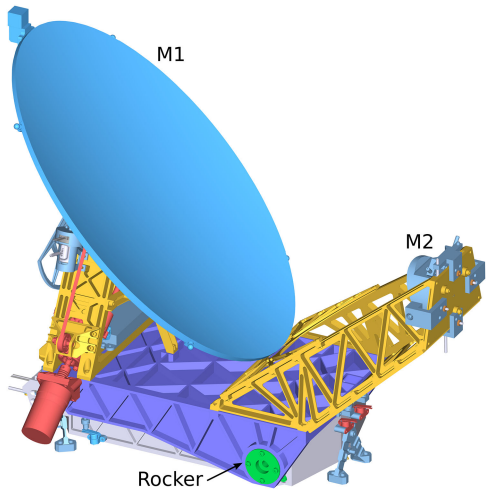

Fig. 1. CAD-model of the SWI TRU.

The scientific objectives of SWI include the investigation of the temperature distribution, chemical composition, and dynamics of Jupiter's stratosphere as well its coupling to other atmospheric regions. The atmospheres, their interaction with the Jovian magnetosphere, and the surface properties of the icy moons Callisto, Europa, and Ganymede will be characterized as well. SWI will therefore provide information that is complementary to the data provided by the microwave radiometer (MWR) on the Juno spacecraft [2] that is currently performing observations of lower parts of Jupiter's atmosphere in the frequency band 0.6–22 GHz. Other microwave radiometers flown on past missions for investigating solar system objects include the Microwave Instrument on Rosetta Orbiter [3] and the RADAR multimode instrument on Cassini spacecraft [4].

Building on the work presented in [5], this paper first presents the optical design and analysis of SWI in Section II, and then discusses different factors that cause the optical performance of a real instrument to deviate from that of an ideal one in Section III. These factors include manufacturing tolerances that affect the shape accuracy of the optical surfaces, mounting tolerances, as well as deformation and misalignment by thermoelastic effects. The Monte Carlo method has been employed successfully in mounting tolerance analyses of submillimeter-wave instruments [6], [7], and we have adopted the same approach in this paper.

Manuscript received June 21, 2018; accepted August 7, 2018. Date of publication August 20, 2018; date of current version December 11, 2018. The work at the University of Bern was supported in part by the Swiss National Science Foundation under Grant 200020-165744 and in part by the ESA PRODEX program. *(Corresponding author: Mikko Kotiranta.)*

M. Kotiranta, K. Jacob, H. Kim, and A. Murk are with the Institute of Applied Physics, University of Bern, Bern 3012, Switzerland (e-mail: mikko.kotiranta@iap.unibe.ch; karl.jacob@iap.unibe.ch; hyunjoo.kim@iap.unibe.ch; axel.murk@iap.unibe.ch).

P. Hartogh is with the Max Planck Institute for Solar System Research, Göttingen 37077, Germany (e-mail: hartogh@mps.mpg.de).

Color versions of one or more of the figures in this paper are available online at http://ieeexplore.ieee.org.

Digital Object Identifier 10.1109/TTHZ.2018.2866116

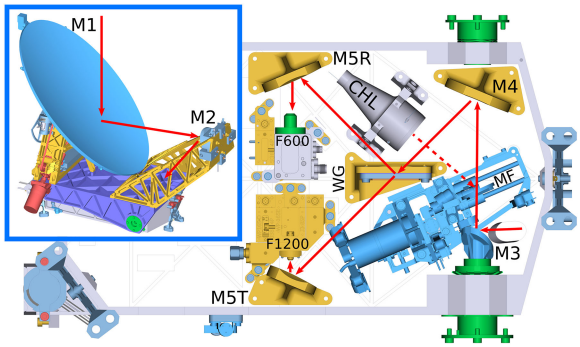

Fig. 2. Beam path in the RU box (view from below, components attached to the top cover).

II. Optical Design

SWI receives the signal of interest with an off-axis Cassegrain telescope. The paraboloidal main mirror (M1) has a projected diameter of 29 cm, whereas the hyperboloidal secondary mirror (M2) has a projected diameter of 6 cm. The telescope is mounted on a rocker that can be tilted $\pm 4.3°$ to allow scanning perpendicular to the spacecraft orbital plane (cross track). Scanning in the orbital plane (along track) is possible by rotating the mirror M1 up to $\pm 72°$. The scanning mechanisms enable observations along Jupiter's limb, mapping of the icy moons with variable incidence angles and polarizations, as well as the use of cold sky for instrument calibration without the need for spacecraft maneuvers.

The beam from the mirror M2 is directed into the RU box through a cutout in the rocker. The contents of the RU box are shown in Fig. 2. After entering the RU box, the beam encounters a planar mirror M3 and an elliptical mirror M4 that reside on the rotational axis of the rocker structure. As the telescope is steered in the cross-track direction, the mirror M3 rotates together with the rocker and the telescope in such a way that the remaining beam path inside the RU box remains fixed. A free-standing wire grid (WG) with a wire diameter of 10 μm and a pitch of 25 μm splits the beam into two orthogonal linear polarizations. The transmitted polarization component that is perpendicular to the wires is reflected from the elliptical mirror M5T to the feedhorn of the 1200-GHz double sideband (DSB) Schottky-mixer receiver [8]. The reflected polarization component parallel to the wires is coupled via the elliptical mirror M5R to the feedhorn of the 600-GHz DSB Schottky-mixer receiver [9]. The less sensitive 1200-GHz receiver is placed in the transmitted beam path because the degrading effect of WG nonplanarity on the transmitted beam is smaller. A corrugated feedhorn is employed in the 600-GHz receiver due to its superior performance as a Gaussian beam source. Although possible [10], manufacturing of corrugated horns is very challenging above 1 THz, and hence a smooth-walled spline-profiled feedhorn is used in the 1200-GHz receiver instead.

A conical blackbody calibration target (CHL) [11] acts as the hot temperature reference during the instrument calibration. To allow the receivers to view the CHL, the beam between M3 and M4 is redirected by activating a planar flip mirror.

TABLE I
Results of Gaussian Beam Mode Analysis

Comp.	f (mm)	d (mm)	R_{in} (mm)	R_{out} (mm)	w_i (mm)	$2\theta_i$ (deg)
M1	348.937	300.0	348.937	inf	98.848 98.872	90
M2	-64.0	241.0	209.179	-49.006	13.874 13.869	53.646
M3	inf	89.414	inf	inf	3.758 2.663	80.839
M4	59.714	72.186	105.854	136.998	9.081 8.397	45
WG	inf	92.814	inf	inf	3.108 3.108	90
M5R M5T	19.759 12.630	25.0 14.681	27.372 16.067	71.048 59.049	6.287 4.276	45 45

The optical design is based on the Gaussian beam mode analysis [12], and further refinements have been carried out with physical optics (PO) simulations with the GRASP software package [13]. The design and the simulations presented in the following subsections assume room temperature conditions.

A. Gaussian Beam Mode Analysis

Frequency-independent operation has been one of the main design drivers that is achieved by imaging the aperture of the feedhorn onto the aperture of the primary mirror M1. In terms of Gaussian beam mode analysis, this means that the Gaussian beam phase shift between the feedhorn and M1 should be a multiple of π [14]. Another constraint for the design is the edge taper requirement of at least 17 dB at M1 that together with the mirror diameter defines the maximum Gaussian beam radius.

The properties of the Gaussian beams launched by the 600- and 1200-GHz feedhorns have been obtained by first computing their far-field radiation patterns at the center and edge frequencies of the respective operating bands with the mode matching software CHAMP [15]. Then, the beam radius and the radius of curvature of a Gaussian beam, which has the highest coupling efficiency to the simulated far-field radiation characteristics, have been determined at the feedhorn aperture by a least-squares fit. In case of the 600-GHz corrugated feedhorn, the beam radius is 0.851 mm and the radius of curvature is 8.35 mm. The respective values for the smooth-walled 1200-GHz feedhorn vary in the range 0.478–0.468 mm and 2.482–4.992 mm, depending on the frequency.

Table I presents the properties of the optical components and the results of the Gaussian beam mode analysis. Here, $f = (1/R_{\text{in}} + 1/R_{\text{out}})^{-1}$ is the effective focal length, d is the distance to the previous component, R_{in} and R_{out} are the radii of curvature of the conic mirror sections, w_i is the incident beam radius at 530 (row 1) and 1080 GHz (row 2), and θ_i is the beam incidence angle. In case of M5R (M5T), d is the distance to the 600-GHz (1200 GHz) feedhorn aperture

Figs. 3 and 4 show the Gaussian beam radius and phase shift from the feedhorn aperture to the primary mirror M1 for the

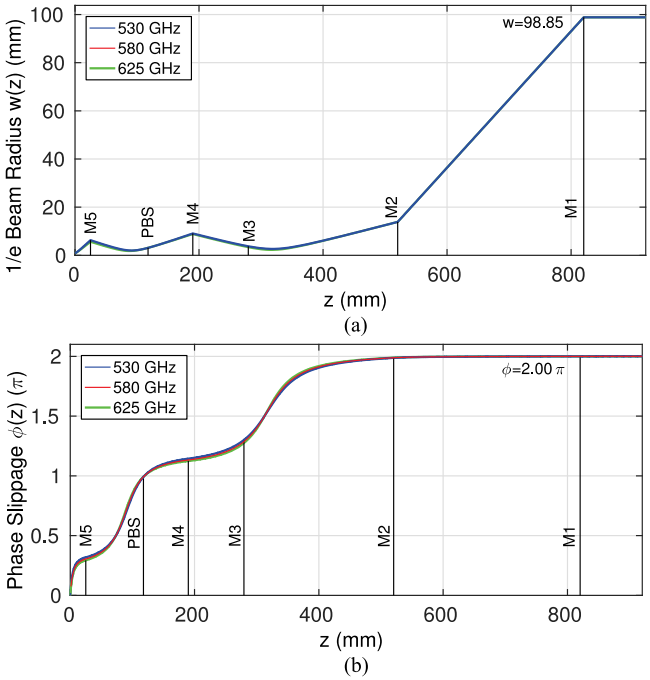

Fig. 3. Gaussian beam mode propagation along the 600-GHz beam path. (a) Radius. (b) Phase shift.

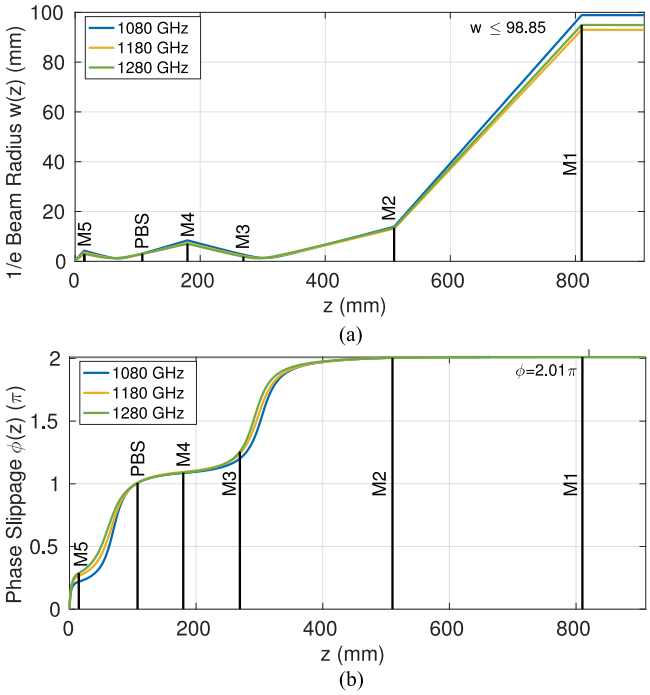

Fig. 4. Gaussian beam mode propagation along the 1200-GHz beam path. (a) Radius. (b) Phase shift.

600- and 1200-GHz channels, respectively. The edge taper at M1 is approximately 18.7 dB, which corresponds to a spillover loss of 1.4%. The beam propagation in the 600-GHz channel is frequency independent, whereas the 1200-GHz channel exhibits some frequency dependence due to the frequency-dependent

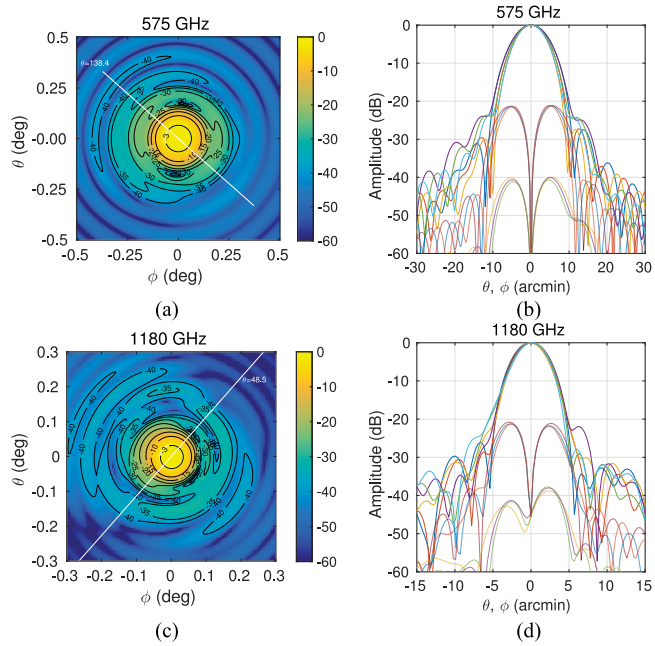

Fig. 5. Simulated SWI far-field radiation patterns: copolar at (a) 575 GHz and (c) 1180 GHz; copolar (solid) and cross polar (dashed) at (b) 530, 575, and 620 GHz, and (d) 1080, 1180, and 1280 GHz. The white lines in (a) and (c) indicate the polarization direction. The patterns in the planes $\theta = 0$ and $\phi = 0$ are included in (b) and (d).

radius and radius of curvature of the input beam that is launched by the smooth-walled feed.

B. PO Analysis

The Gaussian beam mode analysis does not include higher order modes or diffraction. The contribution of these effects has been accounted for in the PO analysis. Instead of the best-fit Gaussian beams, the spherical wave expansions of the actual far-field radiation patterns of the feedhorns originating from the mode matching simulations have been used as an input.

First, the sizes of the optical components inside the RU box have been optimized for minimum spillover loss under mass and space constraints. The final projected radii are $[R_{M3}, R_{M4}, R_{\mathrm{WG}}, R_{M5R}, R_{M5T}] = [10, 19, 10, 16, 12]$ mm. Then, the far-field radiation characteristics of the instrument have been simulated at the edge and center frequencies of each receiver channel. These are shown in Fig. 5 when the telescope scan angles in the cross-track direction ϕ and in the along-track direction θ are zero. This means that when the spacecraft is in Jupiter or Ganymede orbit, the instrument points at the nadir, or, in other words, at the center of the planet or the moon. The key performance parameters are summarized in Table II.

The accumulated coupling efficiency at the mirror M1 η_{M1} is >98%. Such a value is expected when one considers the M1 spillover loss of 1.4% predicted by the Gaussian beam mode analysis. Losses due to the finite electrical conductivity of the optical surfaces are not included in η_{M1}. The maximum sidelobe and cross-polarization levels are below -20 dB. The latter is dominated by M1 because of the 90° bend angle that is

TABLE II
RESULTS OF PO ANALYSIS

Freq. (GHz)	530	575	620	1080	1180	1280
Gain (dB)	62.63	63.41	64.07	68.94	69.21	69.56
η_{M1} (%)	98.14	98.34	98.61	98.02	98.03	98.07
FWHM (arcmin)	8.57	7.84	7.28	4.12	3.96	3.72
Max. cross-pol. level (dB)	-21.19	-21.11	-21.11	-20.80	-21.23	-21.30
Offset $\Delta\phi$ (arcmin)	-0.05	-0.04	-0.03	0.15	0.01	0.16
Offset $\Delta\theta$ (arcmin)	0.03	0.01	0.01	-0.11	-0.04	-0.10

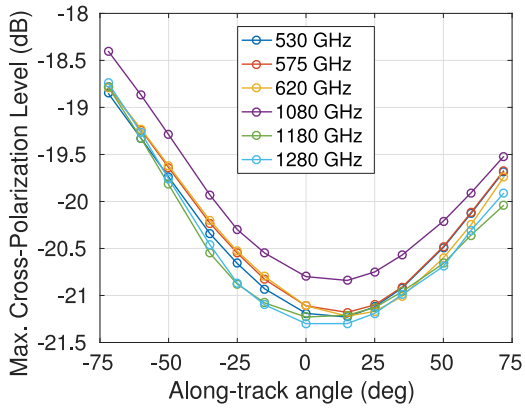

Fig. 6. Simulated maximum cross-polarization level for different along-track scan angles.

inherent to the instrument scanning concept. The instrument pointing offsets were determined by fitting a two-dimensional Gaussian function to the far-field radiation pattern data. The absolute offsets are ≤0.16 arcmin in the along-track and cross-track directions for both 600- and 1200-GHz beams. They are nonzero because of the distortions caused by the off-axis configuration. The requirement set by the science goals is less than 0.5 arcmin, but this also includes the error contribution from the motors of the scanning mechanism and the misalignment and deformation factors discussed in Section III. The boresight directions of the 600- and 1200-GHz beams on the sky agree to within 0.25 arcmin, the requirement being better than 1 arcmin.

The effect of scanning in the cross-track direction is negligible, whereas scanning the instrument in the along-track direction causes the maximum cross-polarization level to increase with increasing absolute scan angle as shown in Fig. 6. The cross-polarization performance of the 1200-GHz feedhorn at the band edge frequency of 1080 GHz is about 0.4 dB worse than the performance at other frequencies. Regardless of the frequency, the cross polarization is below –20 dB for the range –32° to 56°. The pointing offsets, and consequently the coalignment of the beams, change as well, but the absolute errors remain approximately the same as for the nadir pointing.

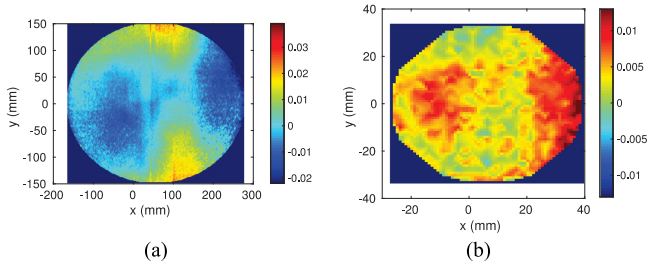

Fig. 7. Difference between measured and ideal surfaces. (a) M1 and (b) M2. The color scale is in millimeters.

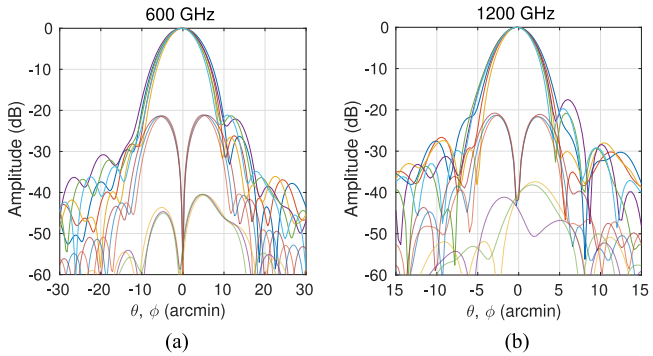

Fig. 8. Simulated SWI copolar (solid) and cross-polar (dashed) radiation pattern cuts at (a) 530, 575, and 620 GHz and (b) 1080, 1180, 1280 GHz using measured M1 and M2 surface profiles. The patterns in planes $\theta = 0$ and $\phi = 0$ are included in (a) and (b).

III. TOLERANCE ANALYSIS

We have investigated different factors that cause the optical performance of the real instrument to deviate from the performance presented in Section II. These factors include manufacturing and mounting tolerances of the optical components, as well as their thermoelastic deformation and misalignment when they are exposed to operational temperatures ranging roughly from –160 °C to –120 °C during the mission.

A. Manufacturing Tolerance

The surface shape accuracies of the M1 and M2 prototypes were characterized with a coordinate measurement machine (CMM). Fig. 7 shows the difference between the measured surfaces and the ideal surfaces, the positions of which have been adjusted to best fit the measured data. The root-mean-square (RMS) difference over the complete surface is about 8 μm and 5 μm for M1 and M2, respectively, or less than $\lambda/29$ at 1280 GHz.

The effect of the nonideal surface shape accuracies has been evaluated by importing the measured point clouds into the optical model and by simulating the far-field radiation performance using the PO method. The results show that the change in the performance parameters of Table II are minor except for the pointing offset $\Delta\phi$ that changes –0.40 arcmin (+0.31 arcmin) at 575 GHz (1180 GHz). In the along-track direction, the absolute change is smaller than 0.10 arcmin. The radiation pattern

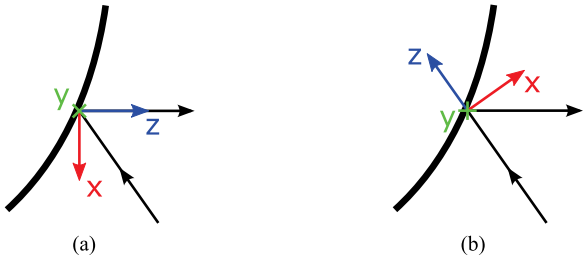

Fig. 9. Local coordinate systems used in the mounting tolerance simulations. (a) Monte Carlo. (b) Individual misalignment of components.

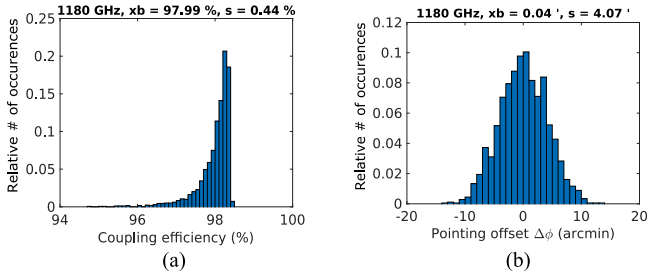

Fig. 10. Histograms of the Monte Carlo analysis for $SD_{in} = 35$ μm/mdeg. (a) Coupling efficiency. (b) Pointing offset $\Delta\phi$.

cuts in Fig. 8 show that the sidelobe level at 1080 GHz rises to above –20 dB.

B. Mounting Tolerance: Monte Carlo Simulations

To evaluate the uncertainty in the predicted optical performance due to mounting tolerances, we have run PO simulations in a Monte Carlo fashion. Each component is assigned random rotational and translational misalignments with respect to a local coordinate system as the one shown in Fig. 9(a). The translational misalignments have two degrees of freedom along *x*-, *y*-, and *z*-axis, whereas the rotational misalignments have two degrees of freedom about the *x*- and *y*-axis. The random values are drawn from a normal distribution with a standard deviation SD_{in}. The mounting tolerance of the components is defined as $2SD_{in}$.

The Monte Carlo simulations have been run for SD_{in} of 20, 35, and 50. The units are either in μm in case of translational or in mdeg in case of rotational misalignment. For each standard deviation, 1800 simulations have been performed. Fig. 10 shows two example distributions obtained at 1180 GHz for $SD_{in} = 35$ μm/mdeg. Fig. 10(a) is the coupling efficiency η_{M1} with a sample mean of 97.99% and standard deviation SD_{out} of 0.44%. The mean value matches closely the performance without misalignment (cf., Table II), and the standard deviation expresses the fact that for a mounting tolerance of 70 μm/mdeg, the coupling efficiency will have an uncertainty of about 0.9% with a probability of 95.45%. The skewness of the distribution indicates that the design is near to the optimum in terms of coupling efficiency. Fig. 10(b) shows the pointing offset $\Delta\phi$. The distribution is roughly symmetric about 0 arcmin, but SD_{out} of 4 arcmin constitutes a significant uncertainty when compared

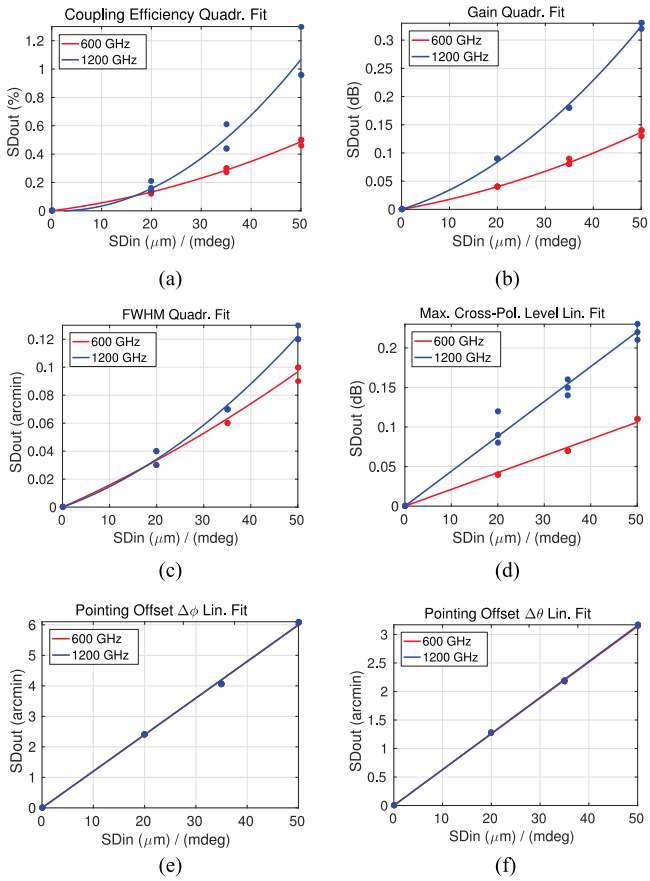

Fig. 11. Standard deviation of the Monte Carlo distributions at edge and center frequencies for different values of SD_{in}. (a) Coupling efficiency η_{M1}. (b) Gain. (c) Full width at half maximum (FWHM). (d) Maximum cross-polarization level. (e) Cross-track pointing offset $\Delta\phi$. (f) Along-track pointing offset $\Delta\theta$.

to the instrument absolute pointing error requirement of 0.5 arcmin.

The standard deviations SD_{out} of the optical performance parameters originating from the Monte Carlo analysis are given in Fig. 11 for the input standard deviations SD_{in} of the normal distribution. For each SD_{in}, the figure shows three data points that are the uncertainties at the edge and center frequencies of the two receiver channels and a curve that has been fitted to these data points. The uncertainty in η_{M1}, FWHM, and gain are nonlinearly dependent on the mounting tolerance, whereas the maximum cross-polarization level and pointing offsets $\Delta\phi$ and $\Delta\theta$ are linearly dependent. The performance uncertainty is higher for the 1200-GHz channel than for the 600-GHz channel, apart from the pointing offsets, in case of which the uncertainties are practically identical.

C. Mounting Tolerance: Individual Misalignment

The alignment of most optical elements in the TRU is fixed by dowel pins and can only be adjusted in one direction by shims. The feedhorns, or rather the mixer blocks to which the feeds are attached, and the mirror M2 are exceptions. By adjusting the position and orientation of these elements, the compensation of, for example, the beam pointing error is possible to some degree.

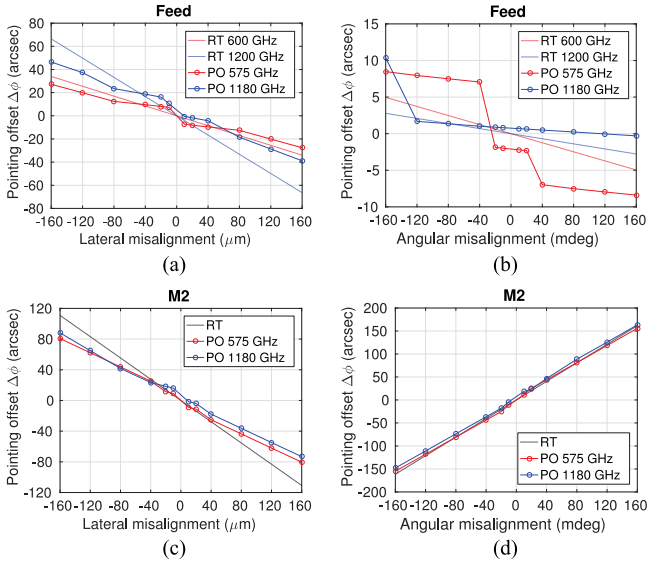

Fig. 12. Simulated effect of misalignment on pointing offset $\Delta\phi$: lateral misalignment of (a) feedhorn and (c) M2, and angular misalignment of (b) feedhorn and (d) M2. The stated frequency refers to the channel in case of RT, which considers only the optical path, whereas in case of PO, it is also the actual frequency of the propagating beam.

Therefore, simulations in which the optical elements are individually misaligned after each other have been performed using the PO method and a faster ray-tracing (RT) method based on ABCD matrices [16]. The misalignment of submillimeter-wave optics has been previously studied with the ABCD matrices in [17] and [18].

Fig. 12 shows the predicted cross-track pointing offset $\Delta\phi$ of the 600- and 1200-GHz beams as the feedhorns or the mirror M2 are individually misaligned by translating the component laterally along the x-axis or by rotating the component around the y-axis of the coordinate system sketched in Fig. 9(b). Both simulation methods yield results with similar characteristics, but the RT method predicts higher sensitivity to the lateral misalignment. The angular misalignment sensitivities of the feedhorns are very small when compared to that of the mirror M2. Very good agreement between two simulation methods is obtained for the angular misalignment sensitivity of M2.

Fig. 12 suggests that correction of the instrument pointing error by more than 1 arcmin is feasible with an adjustable mirror M2. The translation of the feedhorns will help as well. Both correction methods are incorporated into the instrument optical alignment concept. After each adjustment, the component positions are measured with a CMM, and the resulting pointing offsets are determined with near-field beam pattern measurements.

The individual misalignment simulations show that the pointing offsets of the instrument beams are most sensitive to the angular misalignment of the mirror M1: in the along-track direction, the misalignment angle is directly transferred to the offset $\Delta\theta$, whereas in the cross-track direction, the offset $\Delta\phi$ is two times the misalignment angle.

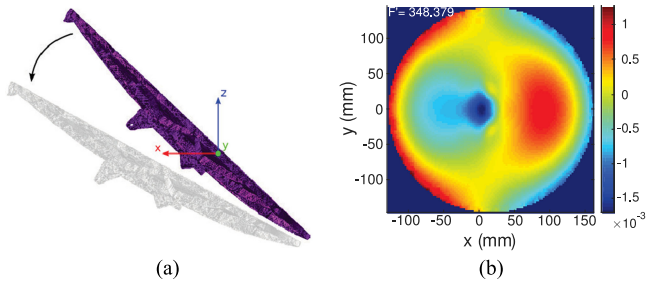

Fig. 13. Cooling of mirror M1 from room temperature to 100 K. (a) Simulated thermoelastic deformation (exaggerated). (b) Difference from a best-fit paraboloid. The color scale is in millimeters.

D. Thermoelastic Deformation

The deformation of the mirror M1 caused by uniform cooling from room temperature down to 100 K has been computed with the finite-element method (FEM). The mirror is assumed to be mounted on a fixture having the same coefficient of thermal expansion as the mirror itself. The cooling causes the mirror to tilt 40 mdeg around the y-axis and to shift –0.29 mm along the z-axis as sketched in Fig. 13(a). The paraboloidal shape of the mirror is preserved upon cooling, but the focal length becomes shorter. Fig. 13(b) shows the difference between the cooled surface and the best-fit paraboloid with a focal length of 348.379 mm: the RMS difference over the complete surface is just 0.5 μm. The tilt in the cross-track direction gives rise to a pointing offset $\Delta\phi$ of about –2 arcmin, regardless of the frequency, when a far-field simulation with the deformed mirror surface is performed. The gain decreases by 0.4–0.5 dB and the FWHM increases by 0.2–0.6 arcmin in the 600-GHz channel. The corresponding changes are 1.5–3.6 dB and 0.3–1.4 arcmin for the 1200-GHz channel.

E. Thermoelastic Misalignment

Thermoelastic FEM simulations of the complete TRU have been performed as well. In these simulations, the TRU was uniformly cooled to temperatures of –100, –130, and –160 °C, and the translational misalignment of the components M1, M2, M3, M4, M5R, M5T, and the feedhorns was determined. The TRU shrinks rather symmetrically, and the maximum translation is about 0.8 mm, which is obtained for the mirror M2. The simulation setup did not yet support the extraction of rotational misalignments or surface deformations.

The component positions at each temperature have been incorporated into the optical model and the instrument far-field performance has been simulated with the PO method. Fig. 14 summarizes the results. Both receiver channels show similar response to cooling. The accumulated coupling efficiency at M1 increases slightly, which is largely due to the shorter net distance between the mirrors M1 and M2 and the consequent reduction in spillover. We also notice a small increase of 0.1–0.2 arcmin in the FWHM and a decrease of 0.2–0.3 dB in gain, which is a sign of beam deformation. The pointing offsets with a maximum magnitude of 1.0–1.5 arcmin are the main effect of the translational misalignments. However, the cooling does not

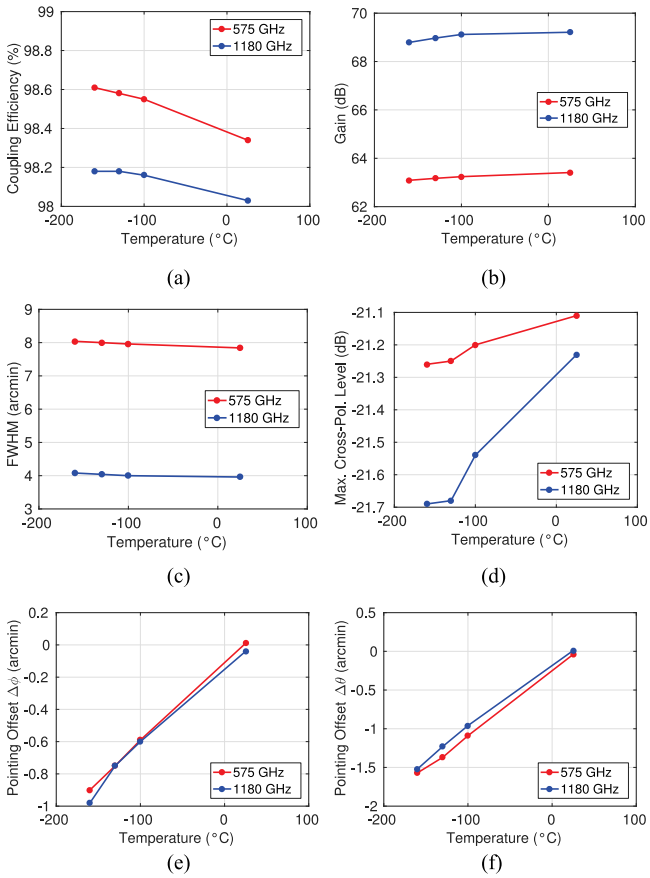

Fig. 14. Simulated optical performance of SWI at different temperatures. (a) Accumulated coupling efficiency η_{M1}. (b) Gain. (c) FWHM. (d) Maximum cross-polarization level. (e) Cross-track pointing offset $\Delta\phi$. (f) Along-track pointing offset $\Delta\theta$.

have much effect on the coalignment of the 600- and 1200-GHz beams since the change in pointing is almost the same for both channels.

IV. Conclusion

We have described the optical design of SWI on the JUICE spacecraft. Frequency-independent operation for the 600-GHz receiver channel has been achieved, whereas some frequency dependence is present in the 1200-GHz channel due to the selected feedhorn type. Scanning of the telescope in the cross-track direction does not influence the optical performance, but along-track scanning increases the cross-polarization level by up to 2.5 dB. However, the maximum levels are obtained for angles at which only cold sky calibration is performed, which is not affected by the cross-polarization level.

Using PO simulations with simulated FEM and measured CMM data as an input to the optical model, we have studied how the surface shape accuracy, component mounting tolerance, as well as deformation and misalignment by thermoelastic effects affect the optical performance of the instrument. The pointing offset of the instrument, which is within the specification for the ideal optical configuration, can be affected up to several arcminutes by these factors. The coalignment of the 600- and 1200-GHz beams is less affected and remains within the specification. By aligning the feedhorns and the mirror M2 during the instrument assembly, one can compensate the pointing error introduced by the other components. However, determination of the operational pointing error with sufficient accuracy before the spacecraft launch is difficult, and hence pointing calibration measurements in the form of planet or moon scans are planned for the cruise and operations phase of the mission.

Acknowledgment

The authors would like to thank the whole SWI team, especially S. Stämm and S. Frahm of the Max Planck Institute for Solar System Research, Göttingen, Germany, for providing the FEM simulation data, and Y. Kasai, S. Ochiai, and Y. Nagai of the National Institute of Information and Communications Technology, Japan, for providing the CMM data of the mirrors.

References

[1] P. Hartogh *et al.*, "The submillimetre wave instrument on JUICE," in *Proc. Eur. Planet. Sci. Congr.*, London, U.K., 2013, Paper EPSC2013-710.
[2] M. A. Janssen *et al.*, "MWR: Microwave radiometer for the juno mission to Jupiter," *Space Sci. Rev.*, vol. 213, no. 1–4, pp. 139–185, Nov. 2017.
[3] S. Gulkis *et al.*, "MIRO: Microwave instrument for rosetta orbiter," *Space Sci. Rev.*, vol. 128, no. 1–4, pp. 561–597, Feb. 2007.
[4] C. Elachi *et al.*, "Radar: The cassini titan radar mapper," *Space Sci. Rev.*, vol. 115, no. 1–4, pp. 71–110, Nov. 2004.
[5] M. Kotiranta, A. Murk, K. Jacob, H. Kim, and P. Hartogh, "Optical design of the submillimeter wave instrument on JUICE," in *Proc. 26th Int. Symp. Space THz Technol.*, Pasadena, CA, USA, 2018, pp. 1–3.
[6] A. Hammar *et al.*, "Optical tolerance analysis of the multi-beam limb viewing instrument STEAMR," *IEEE Trans. THz Sci. Technol.*, vol. 4, no. 6, pp. 714–721, Nov. 2014.
[7] A. Gonzalez and Y. Uzawa, "Tolerance analysis of ALMA band 10 corrugated horns and optics," *IEEE Trans. Antennas Propag.*, vol. 60, no. 7, pp. 3137–3145, Jul. 2012.
[8] A. Maestrini *et al.*, "1080–1280 GHz Schottky receiver for JUICE-SWI with 1600–2600 K DSB receiver noise temperature," in *Proc. Int. Symp. Space THz Technol.*, Pasadena, CA, USA, 2018. [Online]. Available: https://www.nrao.edu/meetings/isstt/
[9] K. Jacob *et al.*, "Characterization of the 530 GHz to 625 GHz SWI receiver unit for the Jupiter mission JUICE," in *Proc. 36th ESA Antenna Workshop*, Noordwijk, The Netherlands, 2015, pp. 1–6.
[10] A. Gonzalez, K. Kaneko, T. Kojima, S. Asayama, and Y. Uzawa, "Terahertz corrugated horns (1.25–1.57 THz): Design, Gaussian modeling, and measurements," *IEEE Trans. THz Sci. Technol.*, vol. 7, no. 1, pp. 42–52, Jan. 2017.
[11] K. Jacob, A. Schröder, M. Kotiranta, and A. Murk, "Design of the calibration target for SWI on juice," in *Proc. Int. Conf. Infrared, Millim., THz Waves*, Copenhagen, Denmark, 2016, pp. 1–2.
[12] P. F. Goldsmith, *Quasioptical Systems*. Piscataway, NJ, USA: IEEE Press, 1998.
[13] TICRA. GRASP 10.5.0. 2015. [Online]. Available: http://www.ticra.com/software/grasp
[14] J. W. Lamb, "Low-noise, high-efficiency optics design for ALMA receivers," *IEEE Trans. Antennas Propag.*, vol. 51, no. 8, pp. 2035–2047, Aug. 2003.
[15] TICRA. CHAMP 3.1.1. 2014. [Online]. Available: http://www.ticra.com/software/champ
[16] A. E. Siegman, "Ray optics and ray matrices," in *Lasers*. Sausalito, CA, USA: Univ. Sci. Books, 1986.
[17] B. Lazareff and S. Sakamoto, "Alignment tolerances for ALMA optics," ALMA Memo 395, Oct. 25, 2001.
[18] M. Candotti, Y. Uzawa, S. V. Shitov, Y. Fujii, and K. Kaneko, "ALMA band 10 optics tolerance analysis," in *Proc. Int. Symp. Space THz Technol.*, Groningen, The Netherlands, 2008, pp. 521–527.

Mikko Kotiranta (S'11–M'13) received the M.Sc. (Tech.) degree (Hons.) in electrical engineering from the Helsinki University of Technology, Espoo, Finland, in 2008, and the Ph.D. degree in physics from Goethe University of Frankfurt, Frankfurt am Main, Germany, in 2013.

He was with Fraunhofer Institute for Applied Solid State Physics IAF, Freiburg im Breisgau, Germany, from 2013 to 2015, as a Monolithic Microwave Integrated Circuit (MMIC) Designer and, from 2014, as the Head of the Device Modeling Group. He was involved in the design and modeling of microwave and millimeter-wave MMICs for cryogenic applications. In 2015, he joined the Institute of Applied Physics, University of Bern, Bern, Switzerland, where he is engaged in the development of quasi-optical components and systems at submillimeter wavelengths for atmospheric and astrophysical research.

Karl Jacob received the M.Sc. degree in physics from Albert-Ludwigs Universität Freiburg im Breisgau, Freiburg im Breisgau, Germany, in 2014. He is currently working toward the Ph.D. degree in physics at the University of Bern, Bern, Switzerland.

Since 2014, he has been with the Institute of Applied Physics, University of Bern. His research interests include development and characterization of submillimeter-wave instrumentation.

Hyunjoo Kim, photograph and biography not available at the time of publication.

Paul Hartogh received the M.Sc. and Ph.D. degrees in physics from the University of Göttingen, Göttingen, Germany, in 1985 and 1989, respectively.

He has been a Staff Member with the Max Planck Institute for Solar System Research, Göttingen, since 1990. He developed microwave and far infrared instrumentation for observations of the earth and extraterrestrial atmospheres. He was the Principal Investigator of the Herschel solar system observation program on "Water and Related Chemistry in the Solar System" and is currently the PI of the submillimeter wave instrument on the Jupiter icy moon explorer. He was a Co-Investigator (Co-I) of the Microwave Atmospheric Sounder on Space Shuttle (Atlas 1–3) and is currently the Co-I of the Microwave Instrument for the Rosetta Orbiter, the German receiver for astronomy at THz frequencies on the Stratospheric Observatory For infrared astronomy, he is a member of the Science Definition Team of ESA's M4 mission Atmospheric Remote-Sensing Exoplanet Large-Survey.

Axel Murk was born in Bad Tölz, Germany, in 1968. He received the M.Sc. degree in physics from the Technical University of Munich, Munich, Germany, in 1995, and the Ph.D. degree in physics from the University of Bern, Bern, Switzerland, in 1999.

Since 1999, he has been involved in the development and characterization of submillimeter-wave instrumentation for different ground-based and spaceborne projects. In 2003, he joined the Japan Aerospace Exploration Agency, as an Invited Scientist. Since 2006, he has been the Head of the Terahertz Optics Group, Institute of Applied Physics, University of Bern. His research interests include antenna design and measurements at frequencies in the millimeter- and submillimeter-wave range, quasi-optics, remote sensing, and radio astronomical instrumentation.